Electronic Supplementary Information

Triplet properties and intersystem crossing mechanism of $PtAg_{28}$ nanocluster sensitizers achieving low threshold and efficient photon upconversion

Masaaki Mitsui* and Atsuki Uchida

Department of Chemistry, College of Science, Rikkyo University, 3-34-1, Nishiikebukuro, Toshima-ku, Tokyo, 171-8501, Japan.

Corresponding author

*E-mail: mitsui@rikkyo.ac.jp

Contents

A. Experimental

Reagents. Silver nitride ($AgNO_3$, 99.8+%); methanol (99.8%); dichloromethane (DCM, 99.5+%); and *n*-hexane (96.0+%); were purchased from FUJIFILM Wako Pure Chemical Corp. 1,3-Benzenedithiol (BDT, >95.0%); hydrogen hexachloroplatinate(IV) hexahydrate ($H_2PtCl_6 \cdot 6H_2O$, 98.5+%); sodium borohydride ($NaBH_4$, >95.0%); 2,4-dimethylbenzenethiol (DMBT, >96.0%); perylene (>99.0%, purified by sublimation); azulene (>99.0%); 9,10-diphenylanthracene (DPA, >99.0%, purified by sublimation); 9,10-bis(phenylethynyl)anthracene (BPEA, >98.0%); benz[a]anthracene (>98.0%); and tetracene (>99.0%, purified by sublimation) were purchased from Tokyo Chemical Industry Co., Ltd. Toluene (99.5%); acetone (99.5%); ethyl acetate (99.5+%); *N*,*N*-dimethylformamide (DMF, 99.8%); ethanol (99.5%); rubrene (99.99%); platinum(II) octaethylporphine (PtOEP); and *N*,*N*'-bis(2,5-di-*tert*-butylphenyl)-3,4,9,10-perylenedicarboximide (^{t}Bu-PDI, 97%) were purchased from Sigma-Aldrich Co. LLC. Ultrapure water (resistivity ≥ 18.2 MΩcm) was produced using a Direct-Q UV distillation system. All reagents were used as received.

Synthesis of $Na_4[PtAg_{28}(BDT)_{12}]$. The $Na_4[PtAg_{28}(BDT)_{12}]$ nanocluster (NC) was synthesized utilizing the ligand-exchanging induced size transformation (LEIST) technique.[1] The process began with the synthesis of $Na_2[PtAg_{24}(DMBT)_{18}]$ precursor based on a reported method with slight modification.[2] 30 mg of $AgNO_3$ was dissolved in 5 mL of methanol and 15 mL of ethyl acetate. The solution was then combined with 257 μL of a 30 mM H_2PtCl_6 methanol solution. After 15 minutes of stirring, 100 μL of DMBT was added into the solution, resulting in a yellow suspension. Following this, $NaBH_4/H_2O$ (20 mg / 1 mL) was added, and after 24 hours of stirring, the color of the solution was changed from a brownish black to a green hue. Subsequently, the solvent was evaporated, *n*-hexane was added to eliminate unreacted thiol and byproducts, and the precipitate was washed with ultrapure water. $Na_2[PtAg_{24}(DMBT)_{18}]$ was extracted from the precipitate by adding methanol. This precursor was then further transformed into the target $Na_4[PtAg_{28}(BDT)_{12}]$ using the LEIST technique. For this conversion, 5 mg of $Na_2[PtAg_{24}(DMBT)_{18}]$ was dissolved in 10 mL of methanol, to which 20 μL of BDT was added. The change in color from green to orange indicated successful cluster

transformation. After an hour of stirring, the solution was condensed through evaporation. The removal of the unreacted BDT and released DMBT was accomplished by washing the condensed solution with *n*-hexane, toluene, and DCM multiple times. The $[PtAg_{28}(BDT)_{12}]^{4-}$ NC was ultimately extracted using 1 mL of DMF and stored in the solution because of potential fusion and degradation of the desired cluster in the dry solid state. Subsequently, the DMF solution for various spectroscopic measurements was prepared at the appropriate concentration.

The negative-ion mode ESI-TOF-mass spectrum of the resulting product, depicted in Fig. S1, revealed a peak at 1224.5 *m*/*z*, corresponding to the mass of $[PtAg_{28}(BDT)_{12}]^{4-}$ (**PtAg$_{28}$**) at 1224.5 *m*/*z*. The isotope pattern of the peak closely matched the theoretically obtained one, confirming the successful synthesis of the intended product.

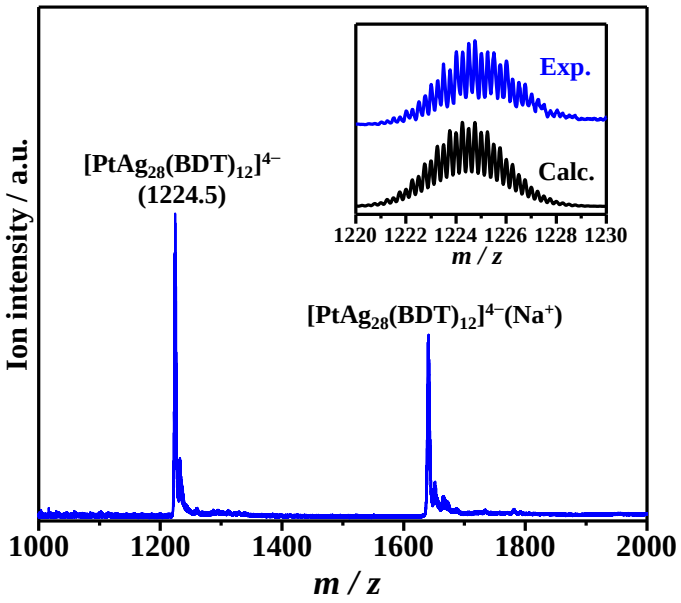

Fig. S1 Negative-ion electrospray ionization mass spectrum of **PtAg$_{28}$** with Na^+ counterions. Inset in shows experimental (blue) and simulated (black) isotopic patterns of **PtAg$_{28}$**.

Electrospray Ionization Time-of-Flight Mass Spectrometry. To characterize the acquired NCs, electrospray ionization time-of-flight mass spectrometry (JEOL, JMS-T100LP AccuTOF LC-Plus) was employed. The NCs, dissolved in a methanol, were subjected to analysis in positive-ion mode.

Mass calibration was performed using a solution of NaI in methanol.

Absorption and Emission Measurements. The ultraviolet–visible (UV–vis) absorption spectrum (Lambda 650 spectrometer, Perkin-Elmer) was recorded within the range of 300–800 nm with a 1 nm interval. The details of the experimental apparatus for emission measurements have been previously described elsewhere.[3,4] In brief, emission spectra were recorded using either a fiber optics spectrometer (USB4000, Ocean optics) or a liquid nitrogen-cooled charge-coupled device camera (Spec-10:100B/LN, Roper Scientific). A continuous-wave laser at 532 nm served as the excitation light source. For emission decay measurements, a picosecond pulsed laser at 478(±6)-nm with a pulse width of 80 ps (PiL048X, Advanced Laser Diode System) was employed. An avalanche photodiode (APD, SPCM-AQRH-61, Perkin-Elmer) was used to record emission decay, and the decay profiles were captured with a time-correlated single photon counting (TC-SPC) card (TimeHarp 260, PicoQuant) and analyzed using SymPhoTime 64 (PicoQuant). Unless otherwise noted, all absorption and emission measurements were implemented in DMF solutions that were fully degassed with high-purity argon gas (> 99.999%).

Evaluation of Emission Quantum Yield. The emission quantum yield (Φ_{em}) was determined using the following equation:

$$\Phi_{em} = \frac{I_r\left(1-10^{-A_r(\lambda_{ex})}\right)}{I_o\left(1-10^{-A_o(\lambda_{ex})}\right)} \frac{\int F_o(\lambda_{em})\,d\lambda_{em}}{\int F_r(\lambda_{em})\,d\lambda_{em}} \frac{{n_o}^2}{{n_r}^2} \Phi_r, \quad \text{(S1)}$$

where subscripts "r" and "o" denote the reference and objective samples, Φ_r is the fluorescence quantum yield of the reference sample, I is the excitation light intensity used in the measurement, and n is the refractive index. $A(\lambda_{ex})$ and $F(\lambda_{em})$ represent the absorbance at the excitation wavelength, λ_{ex}, and the intensity at the emission wavelength, λ_{em}, respectively. A ^{t}Bu-PDI ($\Phi_f = 0.97$)[5] toluene solution was used as the standard sample. As shown in Fig. S2a, the integrated area of the emission spectrum increases linearly with a slope of ~1 concerning laser intensity for both the reference and target samples. To enhance the statistical accuracy of the mean value of Φ_p, 100 values of Φ_p were obtained by substituting all obtained reference and target sample data combinations into eqn (S1). A histogram of

these values was fitted with a Gaussian function, resulting in the determination of the mean and variance of Φ_p (Fig. S2b).

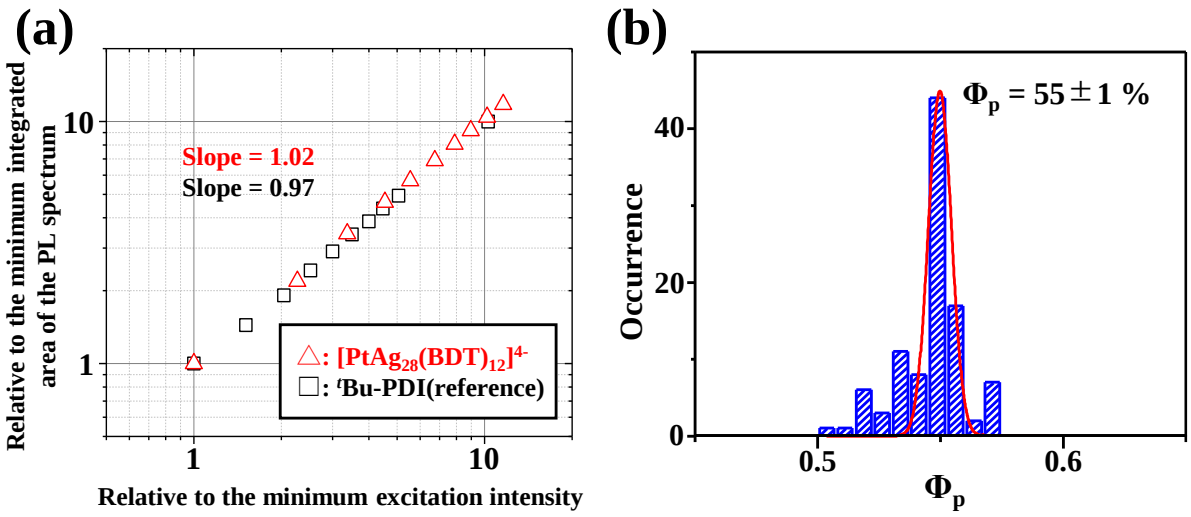

Fig. S2. (a) Dependence of the integrated area of emission spectra of $[PtAg_{28}(BDT)_{12}]^{4-}$ on excitation intensity (λ_{ex} = 478 nm). (b) Histogram of Φ_p values (100 data). The mean value was determined from a Gaussian fit (red solid line).

Transient absorption (TA) spectroscopy. TA measurements were performed using a subnanosecond TA spectroscopy apparatus (picoTAS, UNISOKU Co., Ltd.).[6] The pump source was a picosecond Nd:YAG laser (355 nm, EKSPLA PL-2210A, 1 kHz, fwhm = 25 ps) equipped with an optical parametric generator (EKSPLA PT400, 410−700 nm, 50 μJ/pulse @500 nm), and the probe light source was a supercontinuum radiation source (INDUS FORTE 400, Leukos, 20 MHz, fwhm = 50–100 ps, 410–2400 nm). The time resolution of the system was estimated to be 80–100 ps at a 10−90% rise time. All the measurements were conducted using a quartz cell with an optical path length of 2 mm.

Upconverted emission decay measurements. The experimental setup details have been described elsewhere.[3,4] Briefly, upconverted emission delay profiles were recorded utilizing a pseudo-pulse laser beam created by periodic blocking at 150 Hz through an optical chopper. The emission signals, detected by the avalanche photodiode detector (APD410A/M, Thorlabs), were monitored using an

oscilloscope (TBS1052C, Tektronix) and integrated through custom software developed in LabVIEW2020.

UC threshold intensity measurements. A detailed description of the experimental setup employed for investigating the excitation intensity (I_{ex}) dependence of UC emission intensity (I_{UC}) has already been provided elsewhere.[3] The laser power was monitored by a power sensor-connected power meter (S120C (power range: 50 nW−50 mW), PM100, Thorlabs), and was adjusted incrementally through a variable neutral density filter. In the UC measurement, the excitation laser was focused on the center of the 1.0 × 1.0 cm cuvette, allowing the calculation of the excitation intensity at the cuvette center using the following equation:

$$I_{\mathrm{ex}} = \frac{P \cdot 10^{-A(\lambda_{\mathrm{ex}})/2}}{\pi D^2/4}, \tag{S2}$$

where D is the beam diameter. For 532 nm, D was evaluated to be 0.06 cm. The term $10^{-A(\lambda_{\mathrm{ex}})/2}$ accounts for the decrease in laser power over the 0.5 cm optical path length to the center of the cuvette. The UC emission signal was detected by an APD (SPCM50A/M) after passing through appropriate filters that block other emissions and stray light. The background signal at each excitation intensity was subtracted from the measured emission intensity.

B. TTA-UC Relative Method for Estimating ISC Quantum Yield of PtAg$_{28}$

Lately, we developed a relative method to determine the ISC quantum yield of the sensitizer by leveraging the triplet-triplet annihilation upconversion (TTA-UC) phenomenon.[3,4,7] Herein, this method was employed to evaluate the Φ_{ISC} of **PtAg$_{28}$**. The formation quantum yield of the upconverted state (Φ_{UCs}), i.e., the S_1 state of annihilator/emitter, was expressed as:[7,8]

$$\Phi_{\mathrm{UCs}} = \frac{1}{2}\Phi_{\mathrm{ISC}}\Phi_{\mathrm{TET}} f f_2, \tag{S3}$$

where f represents the spin statistic factor and f_2 is the TTA fraction in the total decay of triplet annihilator (^{3}annihilator*). The f_2 was calculated using the following equation:[9]

$$f_2 = 1 - \frac{\beta - 1}{\beta}\ln(1-\beta), \tag{S4}$$

where β corresponds to the initial fraction of the TTA decay rate (k_{TTA}) over the net decay rate. β can be obtained by analyzing the upconverted emission decay profile, $I_{UC}(t)$, by the following equation:[10]

$$I_{UC}(t) \propto I(0)\left(\frac{1-\beta}{\exp\left(\frac{t}{\tau_T}\right)-\beta}\right)^2, \tag{S5}$$

where $I(0)$ is the upconverted emission intensity at $t = 0$, τ_T is the decay time of ^{3}annihilator* without the contribution of the TTA process. Note that the most accurate fit for $I_{UC}(t)$ was achieved when the β value approached 0.5, avoiding the extremes of $\beta = 0$ and $\beta = 1$.[11] Therefore, the excitation intensity was adjusted to approximate this condition.

The Φ_{UCs} can be evaluated experimentally as[12]

$$\Phi_{UCs} = \frac{\Phi_{UCg}}{(1-\Phi_q)\Phi_F}, \tag{S6}$$

where Φ_q is the quenching yield of ^{3}annihilator* by the sensitizer and Φ_F is the fluorescence quantum yield of the annihilator. Using the TTA-UC system with a known Φ_{ISC} of the sensitizer as a reference, the ratio, Φ_{UCs}/Φ_{UCs}^r, based on eqn (S6) combined with eqn (S3) yielded the following equation:[7,8]

$$\Phi_{ISC} = \Phi_{ISC}^r \cdot \frac{\Phi_{TET}^r f_2^r}{\Phi_{TET} f_2} \cdot \frac{\Phi_{UCg}(1-\Phi_q^r)}{\Phi_{UCg}^r(1-\Phi_q)}. \tag{S7}$$

where subscript "r" indicates the quantity of the reference system. When the same annihilator/emitter and solvent are used in the reference and objective sample systems, f can be considered identical and therefore cancels in eqn (S7). In this study, PtOEP ($\Phi_{ISC}^r = 1.0$) served as the reference sensitizer.[13] A comprehensive evaluation of a series of parameters, necessary for substitution into eqn (S7), was conducted for the PtOEP sensitizer and DPA annihilator/emitter pair in deaerated DMF (Table S2). Under identical experimental conditions, the parameters for the **PtAg$_{28}$**/DPA pair were also evaluated,

leading to the determination of the Φ_{ISC} value for **PtAg$_{28}$**. It should be emphasized that the relative method was not performed under experimental conditions that maximize Φ_{UCg}. The primary focus of this method was on the evaluation of Φ_{ISC} of the sensitizer, and the experimental conditions were tailored accordingly.

Internal UC quantum yield Φ_{UCg}. The internal UC quantum yield Φ_{UCg} was determined using the following equation:

$$\Phi_{UCg} = \frac{I_r\left(1-10^{-A_r(\lambda_{ex})}\right)}{I_o\left(1-10^{-A_o(\lambda_{ex})}\right)} \frac{\int F_o(\lambda_{em})\,d\lambda_{em}}{\int F_r(\lambda_{em})\,d\lambda_{em}} \frac{{n_o}^2}{{n_r}^2} \Phi_r \cdot \frac{1}{\Phi_{out}}, \quad (S8)$$

where Φ_{out} represent the outcoupling yield to compensating for the loss of upconverted photons owing to reabsorption by the sensitizer and emitter molecules. The other terms are the same as in eqn (S1). A ^{t}Bu-PDI ($\Phi_f = 0.97$)[21] toluene solution was used as the standard sample. The wavelength dependence of the detection sensitivity of the CCD spectrometer (USB4000, Ocean optics) on the observed wavelength range was calibrated using a calibration light source. Note that there was little difference in detection sensitivity between the UC emission wavelength range of DPA emitter (420–550 nm) and the fluorescence wavelength range of the reference tBu-PDI dye (500–650 nm).

The Φ_{out} can be calculated using the following equation:[3,4]

$$\Phi_{out} = \frac{\int F_0(\lambda) \cdot 10^{-\frac{A(\lambda)}{2}}\,d\lambda}{\int F_0\,(\lambda)d\lambda}, \quad (S9)$$

where $F_0(\lambda)$ is the emission intensity at a wavelength λ in a dilute solution and $A(\lambda)$ is the absorbance at a wavelength λ of the UC solution, measured under an optical path length of 1.0 cm. In the UC measurement, the excitation laser was focused on the center of the 1.0 × 1.0 cm cuvette, so that the optical path length of the emitted photons is 0.5 cm, and the actual emission intensity observed can be expressed as $F_0(\lambda)\cdot 10^{-A(\lambda)/2}$.

Quenching quantum yield Φ_q. From the measurement of the sensitizer-concentration dependence of the UC emission decay curves, the quenching rate constant (k_q) of ^{3}annihilator* by the **PtAg$_{28}$** sensitizer

was evaluated. The Stern–Volmer plot of the upconverted fluorescence decay rates (τ_T^{-1}) analyzed by the following equation:

$$\frac{1}{\tau_T} = \frac{1}{\tau_{T0}} + k_q[PtAg_{28}] \quad (S10)$$

The quenching quantum yield was then calculated by

$$\Phi_q = \frac{k_q \tau_{T0}[PtAg_{28}]}{1 + k_q \tau_{T0}[PtAg_{28}]} \quad (S11)$$

The results are summarized in Tables S1 and S2 and Fig. S3.

Table S1. UC fluorescence quenching rate constants and triplet lifetime of 9,10-diphenylanthracene (DPA) in deaerated DMF (λ_{ex} = 532 nm).

Sensitizer	Annihilator	k_q / $M^{-1}s^{-1}$	τ_{T0} / ms
$PtAg_{28}$	DPA	1.1×10^6	3.5
PtOEP		9.9×10^7	3.3

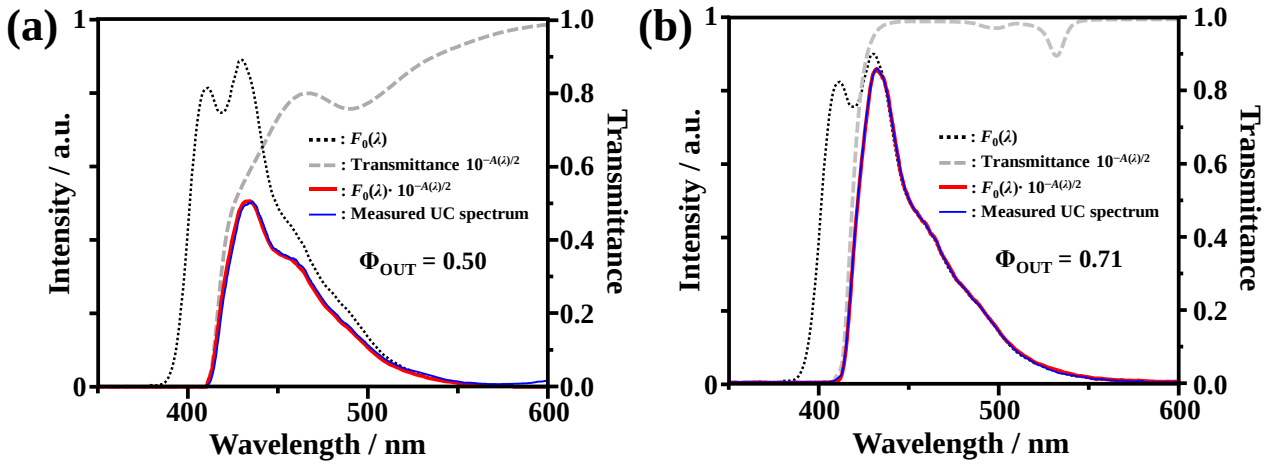

Fig. S3 Dilute solution fluorescence spectra $F_0(\lambda)$ of DPA in DMF. Transmittance curves $10^{-A(\lambda)/2}$ (dashed line), the self-absorption corrected fluorescence spectra $F_0(\lambda) \cdot 10^{-A(\lambda)/2}$, and measured UC fluorescence spectra obtained for (a) **$PtAg_{28}$** (12 μM)/DPA (10 mM) and (b) PtOEP (2.2 μM)/DPA (10 mM) solutions. The value of Φ_{out} obtained from these spectral data and eqn (S9) are also shown.

Table S2. Parameters used in the TTA-UC relative method for estimating the ISC quantum yield of $PtAg_{28}$ sensitizer in deaerated DMF (λ_{ex} = 532 nm).

Sensitizer	[Sen] / μM	Emitter	[Em] / mM	Φ_{UCg} (%)[a]	Φ_{TET}	$1-\Phi_q$ [b]	β	f_2 [c]	Φ_{ISC} [d]
$PtAg_{28}$	12	DPA	10	8.3	0.91	0.97	0.55	0.33	1.03 ± 0.14
	40			5.4		0.91	0.46	0.29	
PtOEP	2.2			7.9	1.0	0.92	0.53	0.34	1.0 [e]
	4.1			5.8		0.88	0.49	0.27	

[a] Calculated by eqn (S8). [b] Calculated by eqn (S11). [c] Calculated by eqn (S4). [d] Calculated by eqn (S7). [e] Reference 13.

C. Oscillator Strength of $T_1 \rightarrow S_0$ Transition

The oscillator strength of the $T_1 \rightarrow S_0$ transition (f_p) was estimated using the following equation for the phosphorescence radiative rate constant:

$$k_r^T = \frac{2\pi e^2 n^3}{\varepsilon_0 m_e h^2 c^3} \Delta E_{T_1-S_0}^2 f_p \,, \tag{S12}$$

where e is the elementary charge, n is the refractive index of the solvent, ε_0 is the dielectric constant in vacuum, m_e is the mass of the electron, h is the Planck constant, c is the speed of light, and $\Delta E_{T_1-S_0}$ is the $T_1 \rightarrow S_0$ transition energy.

D. Emission Quenching Experiments with Aromatic Acceptors

The determination of the rate constants of triplet energy transfer (k_{TET}) involved conducting quenching experiments on the emission lifetimes of **$PtAg_{28}$**, as described by the Stern-Volmer relationship as follows:

$$\frac{\tau_0}{\tau} = 1 + K_{SV}[Q] \tag{S13}$$

where K_{SV} is the Stern−Volmer constant, [Q] is the acceptor concentration, and τ_0 and τ correspond to

the unquenched and quenched emission lifetimes of **PtAg$_{28}$**, respectively. Note that τ_0 corresponds to the phosphorescence lifetime of **PtAg$_{28}$** (i.e., τ_p = 6.8 μs) The k_{TET} was calculated by the following equation:

$$k_{TET} = K_{SV}\tau_0^{-1} \quad \text{(S14)}$$

The results are summarized in Fig. S4 and Table S3.

Table S3. **Phosphorescence quenching parameters of PtAg$_{28}$ obtained with eight different aromatic acceptors in deaerated DMF (λ_{ex} = 478 nm).**

Donor	Acceptor	E_T / eV	K_{SV} / M^{-1}	k_{TET} / $M^{-1}s^{-1}$
PtAg$_{28}$	rubrene	1.14	2.59×10^3	4.54×10^8
	tetracene	1.27	2.25×10^3	3.53×10^8
	perylene	1.53	6.89×10^3	1.03×10^9
	azulene	1.69	4.12×10^3	6.65×10^8
	DPA[a]	1.77	1.40×10^3	2.13×10^8
	anthracene	1.84	1.55×10^3	2.23×10^8
	9-aminoacridine	2.00	4.86×10^2	7.05×10^7
	benz[a]anthracene	2.04	4.19×10	6.10×10^6

[a] 9,10-Diphenylanthracene.

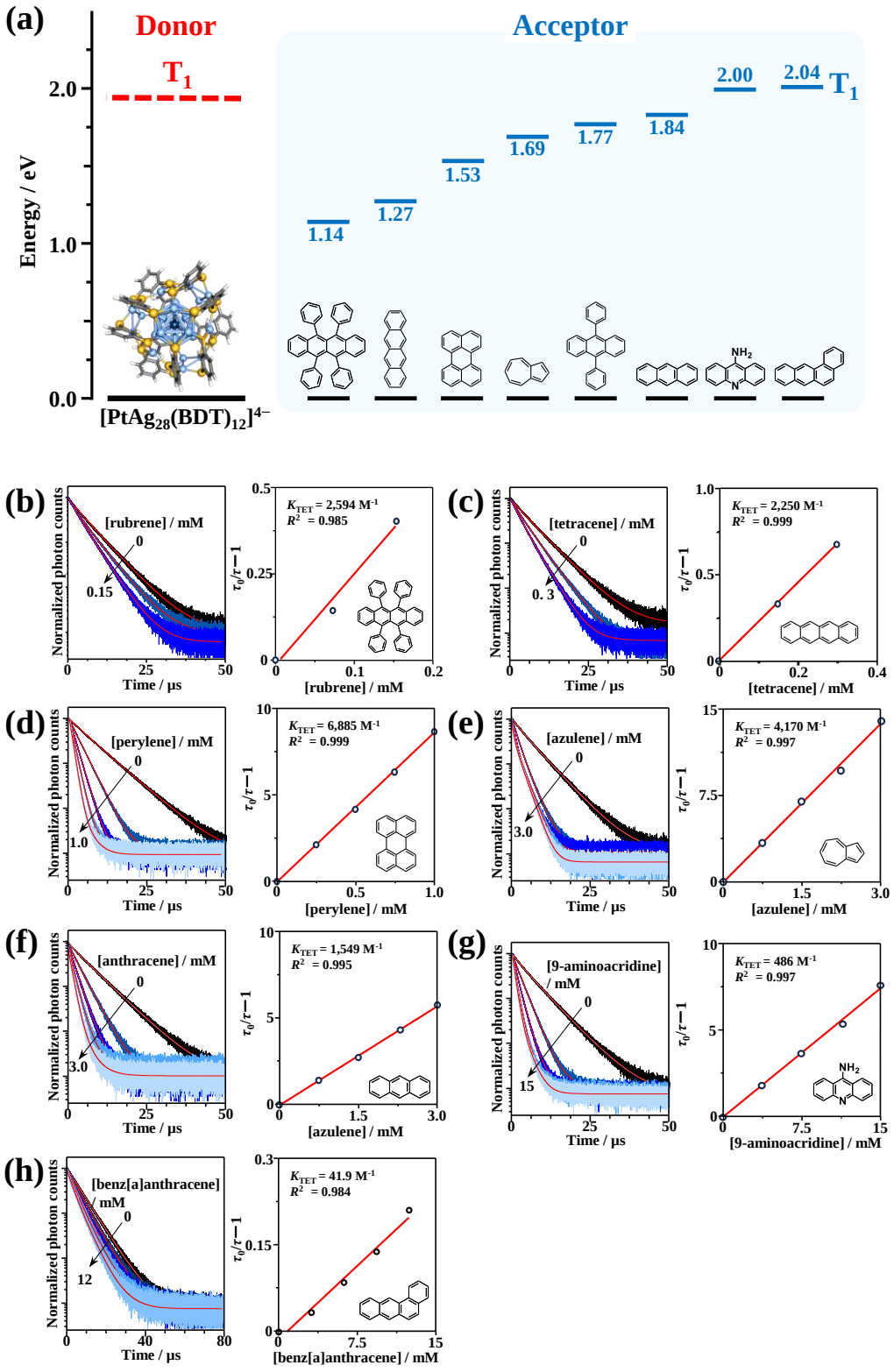

Fig. S4 (a) Energy diagram of $[PtAg_{28}(BDT)_{12}]^{4-}$ (**PtAg$_{28}$**) donor and eight aromatic acceptors combinations. (b–h) Aromatic acceptor concentration dependence of the emission decay curves of **PtAg$_{28}$** (10 μM) in deaerated DMF excited at 478 nm (left). Stern–Volmer plot based on the emission lifetimes (right). The Stern-Volmer constant (K_{SV}) obtained from a linear least-squares fit is also shown. Note that results for the DPA acceptor are shown in Fig. 2a.

E. Analysis of Transient Absorption Kinetics

The transient absorption (TA) kinetics of **$PtAg_{28}$** shown in Fig. 2c were analyzed using the fitting procedure described below.[14]

When the triplet energy transfer (TET) from $^3D^*$ to the ground-state acceptor (A), the rate equations for $^3D^*$ and $^3A^*$ respectively are written:

$$\begin{cases} \dfrac{d[^3D^*]}{dt} = -\left(k_{T(D)} + k_{TET}[A]\right)[^3D^*] & \text{(S15a)} \\ \dfrac{d[^3A^*]}{dt} = k_{TET}[A][^3D^*] - k_{T(A)}[^3A^*] - k_{TTA(A)}[^3A^*]^2 & \text{(S15b)} \end{cases}$$

In eqn (S15a), k_D, k_{TET}, and [A] represent the unimolecular deactivation rate constant of $^3D^*$, the TET rate constant from $^3D^*$ to A, and the acceptor concentration, respectively. In eqn (S155b), k_{A1} and k_{A2} are unimolecular deactivation and second-order rate constant for the bimolecular annihilation process between $^3A^*$, respectively. The $^3D^*$ concentration at time t, which is the solution of eqn (S15a), is written as

$$[^3D^*]_t = [^3D^*]_0 \exp\left(-\frac{t}{\tau_{T(D)}}\right) \quad \text{(S16)}$$

, where $\tau_{T(D)} = \left(k_{T(D)} + k_{TET}[A]\right)^{-1}$. Substituting eqn (S16) into eqn (S15b) yields the following equation:

$$\frac{d[^3A^*]}{dt} = k_{TET}[A][^3D^*]_0 \exp\left(-\frac{t}{\tau_{T(D)}}\right) - k_{T(A)}[^3A^*] - k_{TTA(A)}[^3A^*]^2 \quad \text{(S17)}$$

Note that the initial condition for eqn (S17) is $[^3A^*]_0 = 0$ at $t = 0$. Since eqn (S17) corresponds to a Riccati's differential equation and it is difficult to obtain analytical solution, we attempted to obtain a numerical solution for $[A^*]_t$ using the Runge-Kutta method. The time evolution of delta absorbance, $\Delta A(\lambda)$, at the probe wavelength λ is expressed as

$$\Delta A(\lambda) = \Delta A_{^3D^*}(\lambda) + \Delta A_{^3A^*}(\lambda) \quad \text{(S18)}$$

Considering the Lambert-Beer law, time trace of $\Delta A(\lambda)$ can be explained as following:

$$\Delta A(\lambda) = \alpha_{D^*}\exp\left(-\frac{t}{\tau_{T(D)}}\right) + \alpha_{A^*}[^3A^*]_t \quad (S19)$$

where α_{D^*} and α_{A^*} represent the proportional constants resulting from the relationship of Lambert-Beer law. In the absence of acceptor (i.e., [A] = 0), the least-squares fitting was performed with only the first term of the eqn (S18), whereas in the presence of acceptor, the second term was also included. The parameters obtained by applying the above analysis to the TA kinetic traces in Fig. 2c are summarized in Table S4. Note that the obtained parameters, $k_{T(A)}$ and $k_{TTA(A)}$, agreed well with the literature values of DPA, i.e., $k_{T(A)} = 3.1 \times 10^3$ s^{-1}, $k_{TTA(A)} = 2.5 \times 10^9$ M^{-1}s^{-1}.[15]

Table S4. Parameters obtained from the analysis of transient absorption kinetic traces of $[PtAg_{28}(BDT)_{12}]^{4-}$ ($PtAg_{28}$) (50 μM) in the presence of 9,10-diphenylanthracene (DPA) (9 mM) in a deaerated DMF solution (λ_{pump} = 532 nm).

Donor	Probe wavelength	$\tau_{T(D)}$ / μs	k_{TET} / 10^8 M^{-1}s^{-1}	$k_{T(A)}$ / 10^3 s^{-1}	$k_{TTA(A)}$ / 10^9 M^{-1}s^{-1}
$PtAg_{28}$	600	0.58	2.2	-	-
	444	0.51 (rise)	1.9	4.0	1.3

F. Free Energy Changes for Charger Transfer (ΔG_{CT})

Free energy changes (ΔG_{CT}) of charge transfer (CT) between **$PtAg_{28}$** and aromatic acceptors can be calculated by the Rehm−Weller equation:

$$\Delta G_{CT} = F\left[E^{ox}_{donor} - E^{red}_{acceptor}\right] - E_T + C, \quad (S20)$$

where F is the Faraday constant, E^{ox}_{donor} and $E^{red}_{acceptor}$ are redox potentials of donor and acceptor, E_T is triplet state energy of donor and C is coulombic interaction energy. The coulombic energy can be estimated by following equation:[16]

$$C = \frac{z_{donor} z_{acceptor} e^2}{\varepsilon_s (R_{donor} + R_{acceptor})} - \frac{e^2}{2}\left(\frac{z^2_{donor}}{R_{donor}} + \frac{z^2_{acceptor}}{R_{acceptor}}\right)\left(\frac{1}{\varepsilon_{ref}} - \frac{1}{\varepsilon_s}\right), \quad (S21)$$

where z represents the charge on donor and acceptor in the CT complex, e is the elementary charge, ε_s

and ε_{ref} are the dielectric constants of the solvent used in the absorption/emission measurements and used in electrochemical measurements, respectively. *R* is the van der Waals radii of donor or acceptor. The van der Waals radius of **PtAg$_{28}$** estimated to be 0.763 nm from the reported crystal structure.[17]

Table S5. Free energy change of charge transfer between PtAg$_{28}$ and aromatic acceptors (A) in DMF estimated using the Rehm–Weller Equation.[a]

Donor	Acceptor	R_{PtAg28} / nm	R_{AA} / nm	ε_{DMF}[b]	E^{ox}_{donnor} / V vs. NHE	$E^{red}_{acceptor}$ / V vs. NHE	E_T / eV	$E_{T(A)}$ / eV	C / eV	ΔG_{CT} /eV
PtAg$_{28}$	rubrene	0.761	0.495	38.25	+0.67	–1.40	1.94	1.14	0.09	+0.01
rubrene	**PtAg$_{28}$**				+1.02	–1.19			–0.15	–0.09
PtAg$_{28}$	tetracene		0.377		+0.67	–1.34		1.27	0.10	–0.05
tetracene	**PtAg$_{28}$**				+1.01	–1.19			–0.17	–0.11
PtAg$_{28}$	perylene		0.383		+0.67	–1.43		1.53	0.10	+0.04
perylene	**PtAg$_{28}$**				+1.09	–1.19			–0.16	–0.03
PtAg$_{28}$	azulene		0.315		+0.67	–1.41		1.69	0.10	+0.03
azulene	**PtAg$_{28}$**				+0.95	–1.19			–0.17	–0.18
PtAg$_{28}$	DPA		0.42		+0.67	–1.70		1.77	0.10	+0.31
DPA	**PtAg$_{28}$**				+1.46	–1.19			–0.16	+0.34
PtAg28	anthracene		0.350		+0.67	–1.71		1.84	0.10	+0.31
anthracene	**PtAg$_{28}$**				+1.33	–1.19			–0.17	+0.20
PtAg$_{28}$	benz[a] anthracene		0.373		+0.67	–1.71		2.04	0.10	+0.40
benz[a] anthracene	**PtAg$_{28}$**				+1.63	–1.79			–0.17	+0.51

[a] The redox potentials of the aromatic molecule acceptors were taken from ref.18. [b] Dielectric constant of DMF

G. Estimation of Diffusion-Limited Rate Constant (k_d)

The diffusion-limited rate constants (k_d) between the **PtAg$_{28}$** NC and aromatic acceptors (A) in DMF were calculated by following equation:

$$k_d = 4\pi N_A (R_{NC} + R_A)(D_{NC} + D_A), \quad \text{(S22)}$$

where N_A is the Avogadro number, R and D are the radius and diffusion coefficient, respectively. D can be estimated using the Stokes−Einstein equation:

$$D = \frac{k_B T}{6\pi\eta R}, \tag{S23}$$

where k_B is the Boltzmann constant, T is the absolute temperature, η is the viscosity of solvent. In Table S6, the k_d calculated using eqn (S22) and the parameters used are summarized.

Table S6. Diffusion-limited rate constants and related parameters between the $PtAg_{28}$ nanoclusters (NC) and aromatic acceptors (A) in deaerated DMF.

NC	R_{NC} / Å [a]	R_A / Å [a]	η_{DMF} / J·dm^{-3}·s	k_d / M^{-1}s^{-1}	k_{max} / M^{-1}s^{-1}
$PtAg_{28}$	7.63	3.2−5.0	8×10^{-7}	$(8.6–9.9)\times10^{9}$	$(4.6 \pm 0.9) \times 10^{8}$

[a] Donors and acceptors assumed to be sphere and estimated using the van der Waals volumes.

H. Theoretical Calculations.

We utilized the Gaussian 16 program (ES64L-G16, RevB.01) for both density functional theory (DFT) and time-dependent (TD)-DFT computations, exploring the geometric and electronic structures of $[PtAg_{28}(BDT)_{12}]^{4-}$.[19] The methods applied have demonstrated reliable outcomes for ligand-protected noble-metal nanoclusters.[3,4,7,8] Structural optimizations for $[PtAg_{28}(BDT)_{12}]^{4-}$ in both ground (S_0) and excited (S_1 and T_1) states employed the BP86 exchange correlation functional.[20] These optimizations utilized def2-SV(P) basis sets for Pt and Ag atoms[21] and 6-31G(d) for H, C, and S atoms[22] and the SDD (Stuttgart/Dresden) pseudopotentials including the scalar relativistic effects.[23] To ensure that all the optimized structures were local minimum structures, harmonic vibration frequency analysis was performed to confirm absence of imaginary frequencies. Additionally, vertical transition energies from the S_1- and T_1-optimized structures to the T_n states (n = 1−5), were computed via TD-DFT employing the B3LYP functional,[24] incorporated with Grimme's dispersion interaction (GD3) developed by Grimme and coworkers.[25] The same aforementioned basis functions and pseudopotentials were used in the single-point TD-DFT calculations. Solvent effect of DMF was

included using linear-response polarizable continuum model (LR-PCM).[26] The geometric structures and molecular orbitals were constructed using GaussView 6.0, and Avogadro 1.2.0. Hole and electron distribution analysis was conducted using the Multiwfn 3.8(dev),[27,28] based on the TD-DFT results provided by the Gaussian 16 program. Spin-orbit coupling (SOC) matrix elements were computed with scalar relativistic corrections using the zeroth-order regular approximation (ZORA)[29,30] Hamiltonian at the TD-B3LYP level in ORCA 5.0.4.[31,32] To accelerate the SOC integrals, the RI-SOMF(1X) was introduced, with the choice of TDA false to compute full TD-DFT calculations. Grimme (DFT-D3) empirical pairwise corrections were incorporated for dispersion forces.[33] SARC-ZORA-TZVP basis sets were specified for Au atoms and ZORA-def2-SVP for C, H, and S atoms.[34] The solvent effect of DMF was factored in using the conductor-like polarizable continuum (C-PCM).[35]

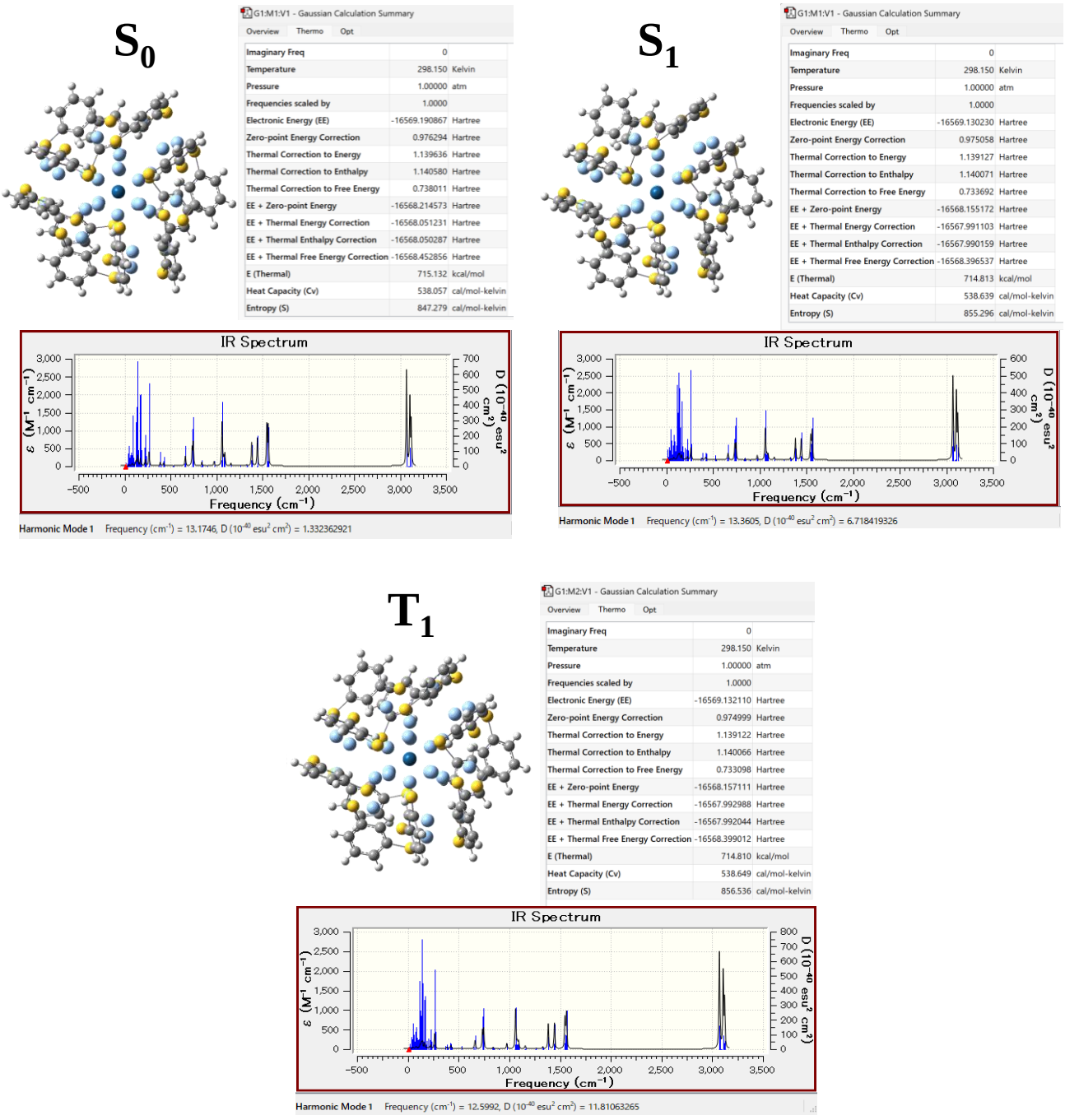

Fig. S5 Optimized structures of $[PtAg_{28}(BDT)_{12}]^{4-}$ in the S_0, S_1, and T_1 states and the corresponding energies. Infrared spectra were obtained by the normal mode analysis.

Table S7. Structural parameters (bond lengths / Å) obtained for the S_0, S_1, and T_1 states of $[PtAg_{28}(BDT)_{12}]^{4-}$.

	S_0	S_1	T_1
Pt(center)-Ag(core)	2.827	2.955	2.968
	2.827	2.800	2.805
	2.827	2.895	2.894
	2.827	2.892	2.895
	2.827	2.788	2.790
	2.827	2.819	2.812
	2.828	2.837	2.872
	2.827	2.843	2.843
	2.827	2.874	2.848
	2.827	2.792	2.792
	2.827	2.789	2.792
	2.827	2.833	2.826
Ag(core)-S	2.588	2.613	2.615
	2.589	2.539	2.541
	2.588	2.616	2.617
	2.588	2.593	2.592
	2.587	2.572	2.573
	2.587	2.558	2.549
	2.587	2.575	2.578
	2.587	2.595	2.595
	2.588	2.621	2.618
	2.587	2.535	2.536
	2.588	2.553	2.545
	2.588	2.612	2.610

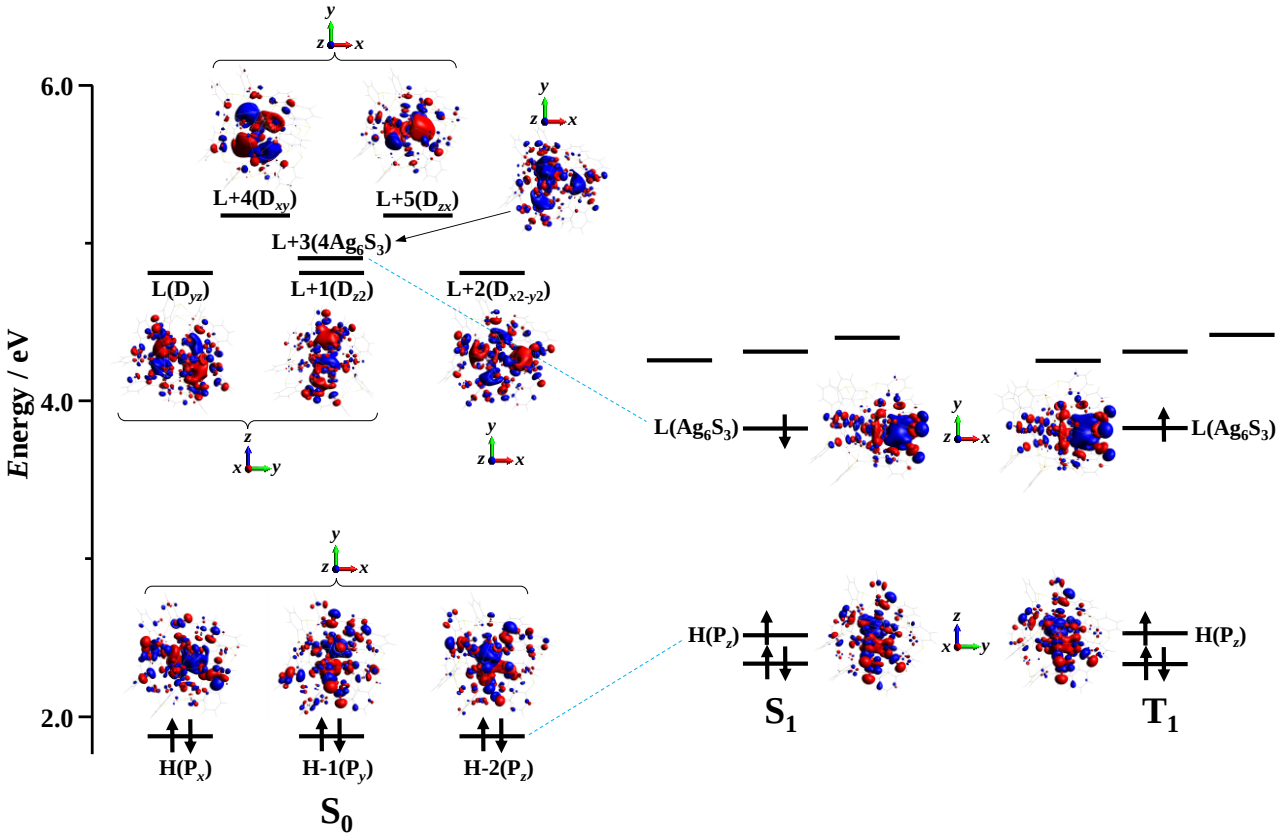

Fig. S6 Energy levels of the frontier molecular orbitals in the ground state (S_0) and the lowest excited singlet (S_1) and triplet (T_1) states of $[PtAg_{28}(BDT)_{12}]^{4-}$. The almost triply degenerate HOMO (H)/HOMO–1 (H–1)/HOMO–2 (H–2) are split by structural symmetry lowering in the S_1 and T_1 states. The symmetry axes of $[PtAg_{28}(BDT)_{12}]^{4-}$ are also shown.

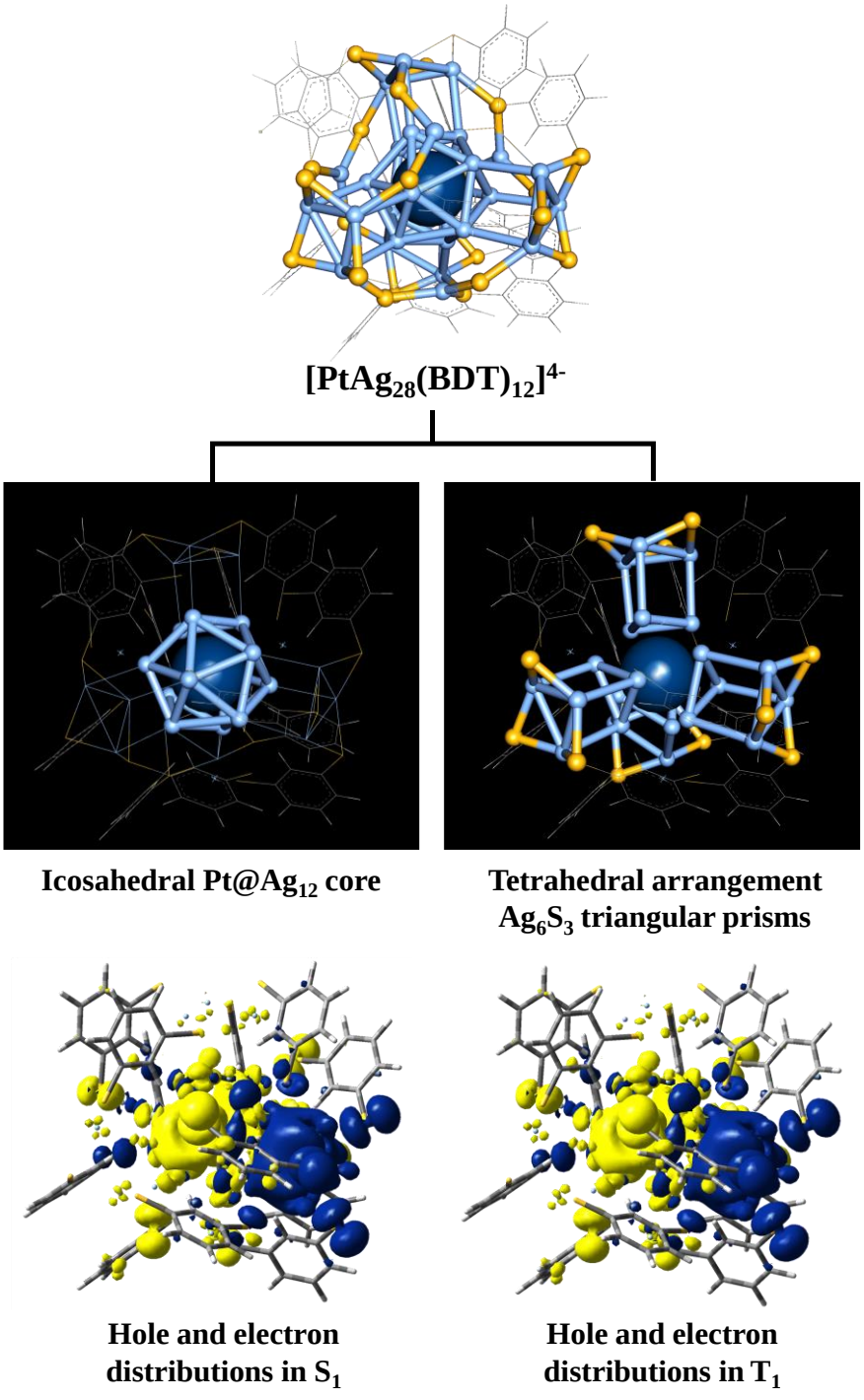

Fig. S7 Schematic highlighting the icosahedral $Pt@Ag_{12}$ core (top left) and Ag_6S_3 (top right) units in $[PtAg_{28}(BDT)_{12}]^{4-}$. The hole and electron distributions in S_1 and T_1 states obtained from TD-DFT calculations (identical to those shown in Fig. 3) are also given in the bottom panel.

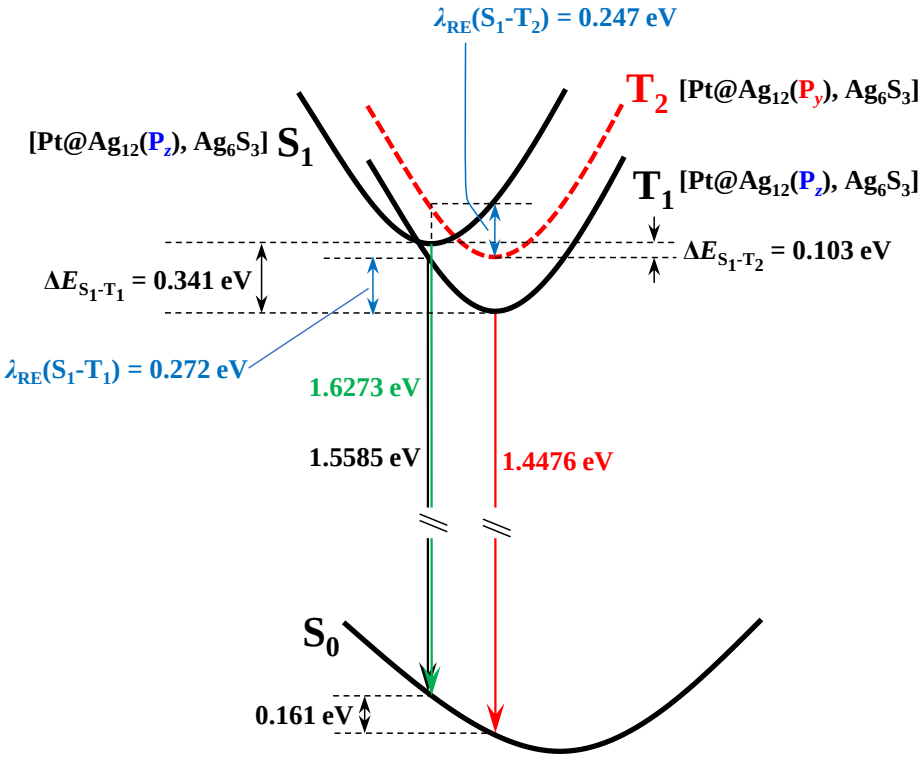

Fig. S8 Schematic potential energy diagram of the S_0, S_1, and T_1 states of $[PtAg_{28}(BDT)_{12}]^{4-}$. The reorganization energy (λ_{RE}) in the S_1–T_1 ISC process obtained by the vertical transition energies (numbers) calculated at the LR-PCM/TD-B3LYP-GD3 level (solvent = DMF) for the S_0-, S_1-, and T_1-optimized structures obtained using BP86 functional.

I. Estimation of ISC Rate Constant

To evaluate the ISC rate constant (k_{ISC}), the ISC rate expression based on the Marcus semiclassical theory[36–38] was used:

$$k_{\mathrm{ISC}} = \frac{2\pi}{\hbar}|V_{\mathrm{SO}}|^2 \frac{1}{\sqrt{4\pi\lambda_{\mathrm{RE}}k_{\mathrm{B}}T}} \exp\left(-\frac{(\Delta E + \lambda_{\mathrm{RE}})^2}{4\lambda k_{\mathrm{B}}T}\right), \tag{S24}$$

where the ΔE is the adiabatic energy gap between the singlet and triplet states and λ_{RE} is the reorganization energy. To account for the contributions of the three spin-sublevels in the triplet state, $|V_{\mathrm{SOC}}|^2$ was averaged using the following equation:

$$|V_{\mathrm{SO}}|^2 = \frac{|\langle \mathrm{T}_n|\hat{H}_{\mathrm{SO}}|\mathrm{S}_1\rangle|^2}{3} = \frac{1}{3}\sum_{i=x,y,z} \left|\langle \mathrm{T}_{n,i}|\hat{H}_{\mathrm{SO}}|\mathrm{S}_1\rangle\right|^2. \tag{S25}$$

Table S8. Spin-orbit coupling matrix elements between the S_1 and T_n (n = 1–4) states in $[PtAg_{28}(BDT)_{12}]^{4-}$ computed at the S_1-optimized geometry. scalar relativistic All-electron calculations with the ZORA at C-PCM/TD-B3LYP-D3 (solvent = DMF) level of theory.

n	$\langle \mathrm{T}_{n,i}\|\hat{H}_{\mathrm{SO}}\|\mathrm{S}_1\rangle$ / cm^{-1}			$\|V_{\mathrm{SO}}\|$ / cm^{-1} [a]
	i			
	x	y	z	
1 [(Pt@$Ag_{12}(P_z)$, Ag_6S_3]	–4.33	19.74	–7.44	12.43
2 [(Pt@$Ag_{12}(P_y)$, Ag_6S_3]	407.47	5.41	113.64	244.25

[a] Obtained using eqn (S25).

Table S9. Estimated intersystem crossing (ISC) rate constants and related parameters.

n	$\Delta E(S_1-T_n)$ / eV [a]	$\lambda_{\mathrm{RE}}(S_1-T_n)$ / eV [a]	$\|V_{\mathrm{SO}}\|$ / eV	$k_{\mathrm{ISC}}(S_1-T_n)$ / s^{-1} [a]
1	0.341	0.272	0.0015	1.1×10^5
2	0.103	0.247	0.030	2.5×10^{11}

[a] Calculated by eqn (S24).

J. UC Measurements under 1-Sun Illumination.

Fig. S9 illustrates the experimental configuration used to measure upconverted emissions under simulated AM1.5G light irradiation, produced by a solar simulator (XES-40S2-CE, San-ei Electric Manufacturing Co., Ltd.). The simulated AM1.5G light intensity was adjusted to 100 mWcm^{-2} using a pyranometer (ML-01, EKO instruments). Optical filters were employed to selectively irradiate the sample solution at wavelengths that do not directly excite the annihilator/emitter molecules. The UC emission spectra were captured by detecting the emission signal with a liquid nitrogen-cooled CCD camera (Spec-10:100B/LN, Roper Scientific).

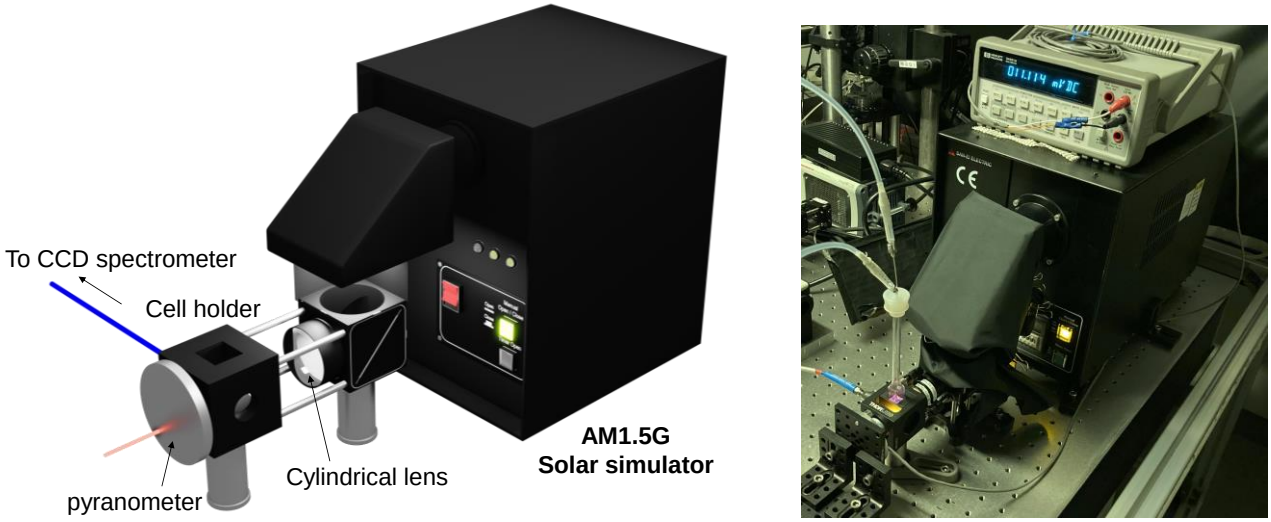

Fig. S9. A computer-generated image and a photograph of the experimental setup for upconversion emission measurements under simulated AM1.5G light illumination.

The excitation rate (k_{ex}), representing the number of photons per second absorbed by a molecule, in monochromatic photoexcitation at wavelength λ, can be determined using the following equation:

$$k_{ex} = \sigma(\lambda)\frac{I_{ex}}{hc/\lambda} = \frac{1000 \cdot (\ln 10)\varepsilon(\lambda)}{N_A}\frac{I_{ex}}{hc/\lambda}, \quad \text{(S26)}$$

where $\sigma(\lambda)$ denotes the absorption cross section at wavelength λ in cm^2, I_{ex} is the excitation laser intensity in Wcm^{-2}, $\varepsilon(\lambda)$ is the molar absorption coefficient at wavelength λ in M^{-1}cm^{-1}, N_A is

Avogadro's constant, c is the speed of light, and h is Planck's constant.

Conversely, when excited by sunlight, the excitation rate is given by the integral (eqn. (S27))[39]

$$k_{\mathrm{ex}} = \int \sigma(\lambda) S(\lambda) d\lambda = \int \frac{1000 \cdot (\ln 10)\, \varepsilon(\lambda)}{N_{\mathrm{A}}} \cdot S(\lambda) d\lambda \qquad \text{(S27)}$$

where $S(\lambda)$ represents the global standard spectrum (AM1.5G) in units of (photon)$s^{-1}cm^{-2}nm^{-1}$. Fig. 1a and Fig. 6b display the spectra of $\varepsilon(\lambda)$ and $\sigma(\lambda)S(\lambda)$, respectively, which were used to calculate the excitation rate of **$PtAg_{28}$** under 1-sun illumination (425–700 nm).

References

1) C. Zeng, Y. Chen, A. Das, and R. Jin, *J. Phys. Chem. Lett.*, 2015, **6**, 2976−2986.
2) X. Kang, M. Zhou, S. Wang, G. Sun, M. Zhu, and R. Jin, *Chem. Sci.*, 2017, **8**, 2581−2587.
3) Y. Niihori, Y. Wada, and M. Mitsui, *Angew. Chem., Int. Ed.*, 2021, **60**, 2822–2827.
4) D. Arima, Y. Niihori, and M. Mitsui, *J. Mater. Chem. C*, 2022, **10**, 4597–4606.
5) S. Prathapan, S. L. Yang, J. Seth, M. A. Miller, D. F. Bocian, D. Holten, and J. S. Lindsey, *J. Phys. Chem. B*, 2001, **105**, 8237–8248.
6) T. Nakagawa, K. Okamoto, H. Hanada, and R. Katoh, *Opt. Lett.*, 2016, **41**, 1498–1501.
7) M. Mitsui, Y. Wada, R. Kishii, D. Arima, and Y. Niihori, *Nanoscale*, 2022, **14**, 7974−7979.
8) D. Arima and M. Mitsui, *J. Am. Chem. Soc.*, 2023, **145**, 6994−7004.
9) Y. Y. Cheng, B. Fückel, T. Khoury, R. G. C. R. Clady, M. J. Y. Tayebjee, N. J. Ekins-Daukes, M. J. Crossley, and T. W. Schmidt, *J. Phys. Chem. Lett.*, 2010, **1**, 1795−71.
10) S. M. Bachilo and R. B. Weisman, *J. Phys. Chem. A*, 2000, **104**, 7711–7714.
11) F. Edhborg, A. Olesund, and B. Albinsson, *Photochem. Photobiol Sci.*, 2022, **21**, 1143−1158.
12) Y. Zhou, F. N. Castellano, T. W. Schmidt, and K. Hanson, *ACS Energy Lett.*, 2020, **5**, 2322−2326.
13) W. Staroske, M. Pfeiffer, K. Leo, and M. Hoffmann, *Phys. Rev. Lett.*, 2007, **98**, 197402.
14) M. Mitsui, D. Arima, Y. Kobayashi, E. Lee, and Y. Niihori, *Adv. Opt. Mater.* 2022, **10**, 2200864.
15) V. Gray, D. Dzebo, A. Lundin, J. Alborzpour, M. Abrahamsson, B. Albinsson, and K. Moth-Poulsen, *J. Mater. Chem. C* 2015, **3**. 11111–11121.
16) M. Mitsui, D. Arima, A. Uchida, K. Yoshida, Y. Arai, K. Kawasaki, and Y. Niihori, *J. Phys. Chem. Lett.*, 2022, **13**, 9272–9278.
17) M. S. Bootharaju, S. M. Kozlov, Z. Cao, M. Harb, M. R. Parida, M. N. Hedhili, O. F. Mohammed, O. M. Bakr, L. Cavallo, and J.-M. Basset, *Nanoscale*, 2017, **9**, 9529–9536.
18) M. Montalti, A. Credi, L. Prodi, and M. T. Gandolfi, *Handbook of Photochemistry, Third ed.*; CRC Press, Boca Raton, 2006.
19) M. J. Frisch, G. W. Trucks, H. B. Schlegel, G. E. Scuseria, M. A. Robb, J. R. Cheeseman, G. Scalmani, V. Barone, G. A. Petersson, H. Nakatsuji et al., Gaussian 16, Revision B.01, Gaussian, Inc., Wallingford CT, 2016.
20) A. D. Becke, *Phys. Rev. A: At., Mol., Opt. Phys.*, 1988, **38**, 3098.
21) F. Weigend and R. Ahlrichs, *Phys. Chem. Chem. Phys.*, 2005, **7**, 3297–3305.
22) M. M. Francl, W. J. Pietro, W. J. Hehre, J. S. Binkley, M. S. Gordon, D. J. DeFrees, and J. A. Pople, *J. Chem. Phys.*, 1982, **77**, 3654–3665.
23) D. Andrae, U. Häußermann, M. Dolg, H. Stoll, and H. Preuß, *Theor. Chim. Acta.*, 1990, **77**, 123 – 141.
24) A. D. Becke, *J. Chem. Phys.*, 1993, **98**, 1372–1377.
25) S. Grimme, J. Antony, S. Ehrlich, and H. Krieg, *J. Chem. Phys.*, 2010, **132**, 154104.
26) B. Xu, Y. Li, P. Song, F. Ma, and M. Sun, *Sci. Rep.*, 2017, **7**, 45688.

27) T. Lu and F. Chen, *J. Comput. Chem.*, 2012, **33**, 580–592.
28) Z. Liu, T. Lu, and Q. Chen, *Carbon*, 2020, **165**, 461–467.
29) E. van Lenthe, E. J. Baerends, and J. G. Snijders, *J. Chem. Phys.*, 1994, **101**, 9783–9792.
30) E. van Lenthe, J. G. Snijders, and E. J. Baerends, *J. Chem. Phys.*, 1996, **105**, 6505–6516.
31) F. Neese, *WIREs Comput. Mol. Sci.*, 2012, **2**,73–78.
32) F. Neese, *J. Chem. Phys.*, 2005, **122**, 034107.
33) S. Grimme, *Comput*. *Mol. Sci.*, 2011, **1**, 211–228.
34) F. Weigend and R. Ahlrichs, *Phys. Chem. Chem. Phys.*, 2005, **7**, 3297–3305.
35) A. V. Marenich, C. J. Cramer, and D. G. Truhlar, *J. Phys. Chem. B*, 2009, **113**, 6378–6396.
36) J. Jortner, *J. Chem. Phys.*, 1976, **64**, 4860–4867.
37) R. A. Marcus, *Rev. Mod. Phys.*, 1993, **65**, 599–610.
38) T. J. Penfold, E. Gindensperger, C. Daniel, and C. M. Marian, *Chem. Rev.*, 2018, **118**, 6975–7025.
39) T. W. Schmidt, F. N. Castellano, *J. Phys. Chem. Lett.* **2014**, *5*, 4062–4072.